Journal of Natural Gas Science and Engineering 81 (2020) 103445

Contents lists available at ScienceDirect

Journal of Natural Gas Science and Engineering

journal homepage: http://www.elsevier.com/locate/jngse

Failure pressure prediction by defect assessment and finite element modelling on natural gas pipelines under cyclic loading

Guojin Qin [a,b], Y. Frank Cheng [a,*]

[a] Department of Mechanical Engineering, University of Calgary, Calgary, Alberta, T2N 1N4, Canada
[b] School of Mechanical Engineering, Southwest Petroleum University, Chengdu, Sichuan, 610500, China

ARTICLE INFO

Keywords:
Pipelines
Corrosion defect
Cyclic loading
Failure pressure
Finite element modelling

ABSTRACT

In this work, a 3-dimensional finite element (FE) model was developed to investigate the effect of cyclic loading, which is induced by vibration during operation of in-line inspection (ILI) tools, on local stress and strain distributions and failure pressure of an X80 steel natural gas pipeline containing a corrosion defect. Modelling was also conducted on a low-grade X60 steel pipe for comparison. Parametric effects, including internal pressure, R-ratio, cyclic frequency and dimension of the corrosion defect (primarily the defect depth), were determined. The cyclic loading greatly increases the von Mises stress and strain at the corrosion defect and reduces the threshold internal pressure to cause plastic deformation at the defect. As the internal pressure increases, both the von Mises stress and the strain increase and the high stress/strain zones expand along the defect length direction. The local stress and strain at the corrosion defect increase with decreased R-ratio and cyclic frequency, resulting in a reduction of failure pressure of the pipeline. An increased defect depth enhances local stress and strain concentrations, reducing failure pressure of the pipeline. A novel method is developed to assess corrosion defect during ILI tool operation and predict the failure pressure of pipelines under cyclic loading for the first time of its kind.

1. Introduction

In-line inspection provides an accurate technique (e.g., magnetic flux leaking or ultrasonic tool) to detect and size various types of defects on pipelines (Vanaei et al., 2017). Defect assessment based on ILI data analysis is an essential component of pipeline integrity management program (API, 2016; Pluvinage, 2008). In the past decade, the authors' group has conducted extensive research on pipeline defect assessment. FE based models were developed to evaluate failure pressure of corroded pipelines and predict the defect growth rate (Xu and Cheng, 2012, 2013, 2017; Sun and Cheng, 2018, 2019a, 2019b). The modelling scope is extensive, including the defect geometry (depth, length and width), steel grade, internal pressure, soil strain, interaction of multiple corrosion defects, stress-corrosion interaction, etc.

During ILI operation, the tool moving inside a pipeline may cause vibration, especially when the tool encounters obstacles such as rough inner wall surface, dents, girth weld between pipe segments, corrosion pits, etc. (Zhang et al., 2015, 2020). Vibration will also happen on pipelines that are suspended on erosive soil supports. The vibration can apply a cyclic loading on the inner wall of the pipeline (Zhang et al., 2015), affecting the local stress and strain distributions at the defect and the failure pressure of the pipeline.

The presence of corrosion defects on pipelines can reduce pipe wall thickness and introduce an additional stress concentration, causing reduction of load-bearing capability of the pipelines (Gong and Zhou, 2018; Abdalla et al., 2014). To date, a wide variety of numerical models and computational codes have been developed for pipeline defect assessment (Xu and Cheng, 2012, 2013, 2017; Sun and Cheng, 2018, 2019a, 2019b; Choi et al., 2003; Ma et al., 2013; Chegeni et al., 2019; Wu and Li, 2019; Mondal and Dhar, 2019; Gong and Zhou, 2017). However, to the authors' best knowledge, none of them has considered the mechanical response due to the ILI-induced vibration and its effect on ocal stress and strain concentrations and the pipeline failure. This work developed a novel method to assess corrosion defect during the ILI tool operation and predict the failure pressure of pipelines under cyclic loading for the first time of its kind.

In this work, a FE model was developed to simulate the stress and strain distributions at a corrosion defect on an X80 steel natural gas pipeline under cyclic loading. A stress-based failure criterion was used to predict the failure pressure of the corroded pipeline. Parametric effects, including internal pressure, defect depth and loading parameters (i.e.,

* Corresponding author.
E-mail address: fcheng@ucalgary.ca (Y.F. Cheng).

https://doi.org/10.1016/j.jngse.2020.103445
Received 1 March 2020; Received in revised form 14 June 2020; Accepted 15 June 2020
Available online 22 June 2020

Nomenclature

CL	Cyclic loading
d	Defect depth, mm
E	Young's modulus, MPa
f	Cyclic frequency, Hz
FE	Finite element
FP	Failure pressure
ILI	In-line inspection
IP	Internal pressure, MPa
K	Constant
L	Defect length, mm
n	Constant
R	Stress ratio
R_p	Outer diameter of the pipe, mm
R_r	Outer diameter of the sealing cup of the ILI tool
RE	Relative error
Q	Constant
t	Pipe wall thickness, mm
$U_{1,2,3}$	Displacement in three principal directions (x-, y- and z-directions)
$UR_{1,2,3}$	Rotation in three principal directions (x-, y- and z-directions)
W	Defect width, mm
ε	Strain
σ	Stress, MPa
σ_y	Yield strength, MPa
σ_u	Ultimate tensile strength, MPa
σ_{Mises}	von Mises stress, MPa
$\sigma_{1,2,3}$	Principal stresses on the pipeline, i.e., hoop stress, longitudinal stress and radial stress, respectively, MPa
σ_{max}	Maximum stresses, MPa
σ_{min}	Minimum stress, MPa

Table 1
Mechanical properties of X60 and X80 pipeline steels.

Steel	Yield strength (MPa)	Ultimate tensile strength (MPa)	Young's modulus (MPa)	Poisson's ratio
X60	433.0	618.0	200,000	0.3
X80	534.1	718.2	200,000	0.3

cyclic frequency and R-ratio), were modelled. For comparison, modelling was conducted on a pipeline made of a low-grade X60 steel.

2. Numerical modelling

2.1. Pipeline steels and geometry of corrosion defect

Both X60 and X80 steel pipes were modelled in this work. They represent the typical low- and high-grades of pipeline steel, respectively. The mechanical properties of the two steels are shown in Table 1. To model a corrosion defect, some simplifications were made so that the results could be applicable for a wide range of geometric shapes. In modified ASME B31G standard, the maximum depth and length along the axial direction of pipeline are used to depict a corrosion defect, which is usually simplified as a rectangular shape (ASME , 1991). In reality, a corrosion defect is characterized by its length L (the longitudinal direction: Z-axis), width W (the circumferential direction: X-axis) and depth d (the pipe wall thickness direction: Y-axis), as shown in Fig. 1a and b. The FE model developed for an internal corrosion defect on the interior of a steel pipe is shown in Fig. 1c and d. The dimension selection of the modelled corrosion defect was based on the industry's corroded pipe database (Norske, 2004; Bipul and Mondal, 2016).

2.2. Initial and boundary conditions

This work used ABAQUS® 6.14 software for FE modelling. A relative tolerance of 0.0001 was adopted to ensure the data convergence. It was assumed that both ends of the pipe segment were under a full consolidation constraint, where the boundary condition can be expressed as

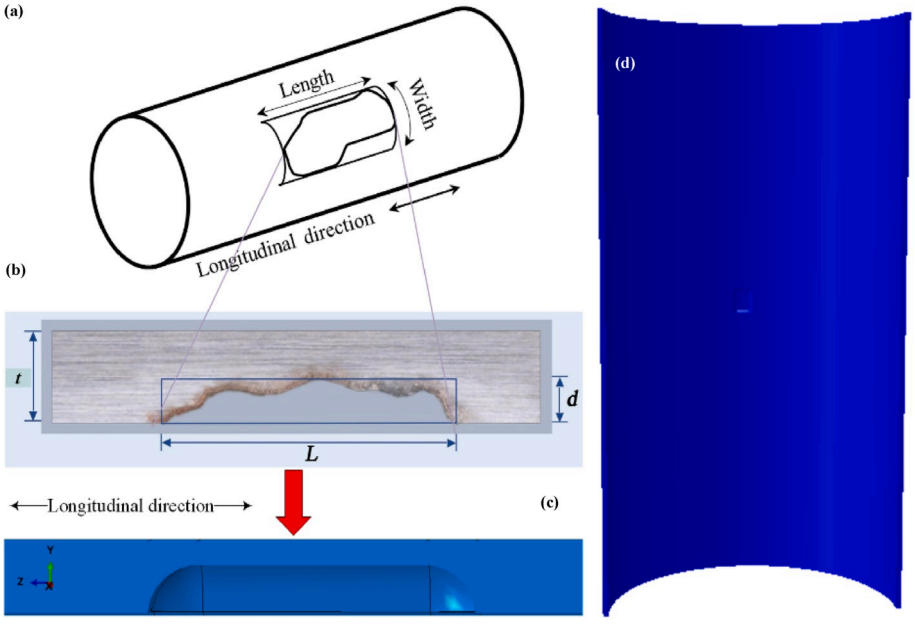

Fig. 1. Schematic illustration of the geometry of a corrosion defect on the interior of a steel pipe and the 3D model for the pipe, where t is the pipe wall thickness, and L, W and d are length, width and depth of the defect, respectively.

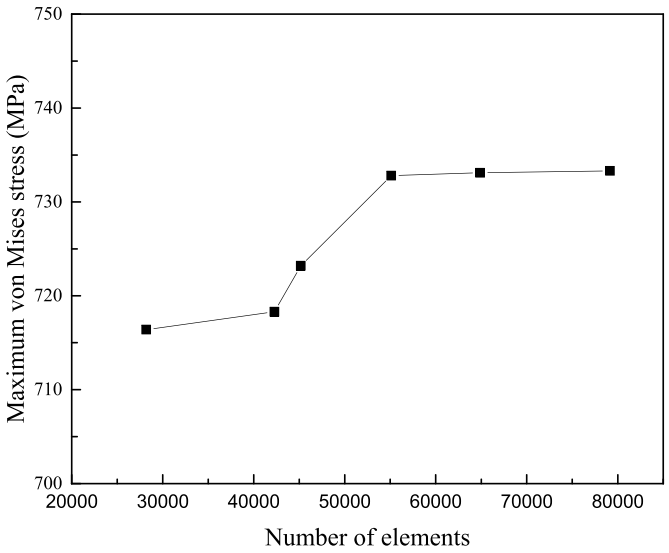

Fig. 2. Mesh density analysis conducted on the modelled corrosion defect.

(Systemes, 2015):

$$U_1 = U_2 = U_3 = UR_1 = UR_2 = UR_3 = 0 \quad (1)$$

where $U_{1,2,3}$ are displacements in three principal directions, i.e., x-, y- and z-directions, respectively, and $UR_{1,2,3}$ are rotations in the three principal directions. The length of the pipe segment was sufficient to avoid the influence of boundary conditions on the corrosion defect, according to Saint Venant's principle.

The steel pipe was modelled by eight-node brick elements with a reduced integration to improve the convergence efficiency for geometrically nonlinear modelling. The FE model with multiple numbers of elements was tested to obtain a reasonable mesh setting so that the modelling results were sufficiently stable and reliable. A mesh density analysis based on the maximum von Mises stress is shown in Fig. 2. The mesh size for the pipe interior was 10 mm in both x- and z-directions, as shown in Fig. 3a. To improve the modelling accuracy, the mesh refinement was performed at the corrosion defect, as detailed in Fig. 3b.

To model the effect of cyclic loading, which is induced by vibration of ILI tools, on failure pressure of the pipeline, a 3-dimensional model was developed, as shown in Fig. 3c, where the sealing cup of the ILI tool advanced along the axial direction (i.e., Z-axis) of the pipe. The diagram of the FE model and the interface between the sealing cup and the pipe are shown in Fig. 3d and e, respectively, where R_p is the outer diameter of the pipe and R_r is the outer diameter of the sealing cup of the ILI tool. The contact between the cup and the pipe was a nonlinear surface-to-surface contact, and the friction coefficient was set as 0.4 (Zhang

Table 2
Five sets of dimension (mm) of the corrosion defect for verification of the developed model in this work.

Number of set	*L*	*d*	*W*
1	36.6	1.62	5
2	39.6	5.39	31.9
3	91.4	3.24	5
4	182.9	4.05	5
5	304.8	4.05	5

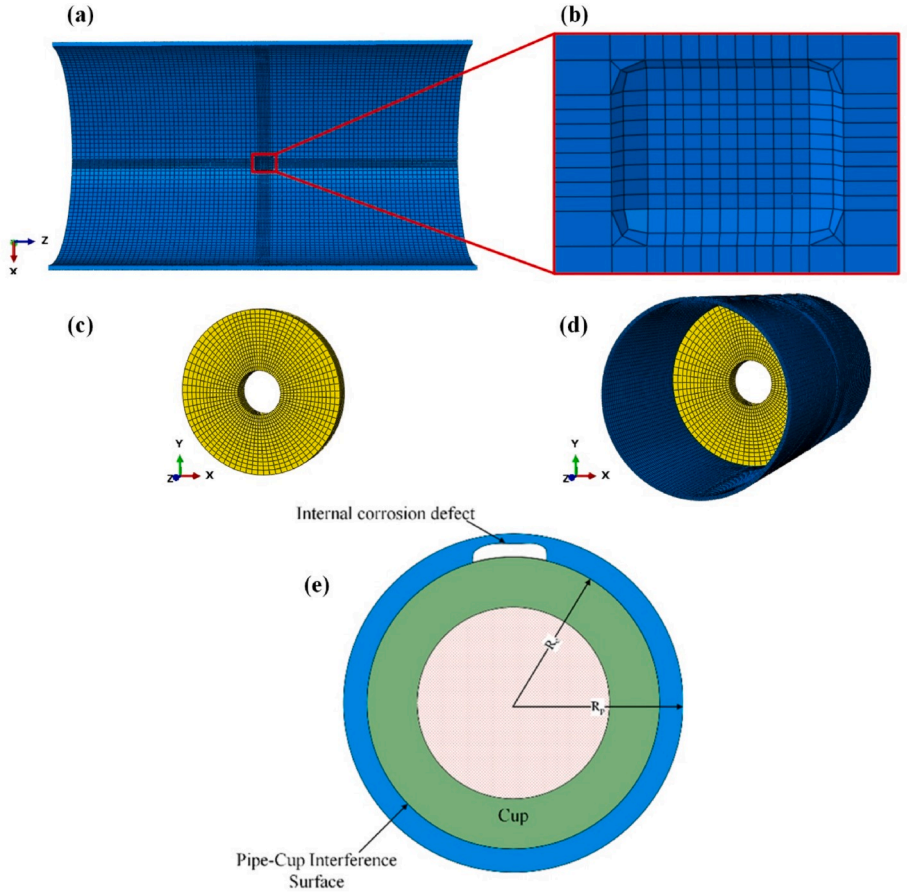

Fig. 3. 3D modelling of a pipe containing an internal corrosion defect (a) meshes of the internal pipe surface, (b) meshes of the corrosion defect, (c) meshes of the sealing cup of an ILI tool, (d) assembly model of the pipe and the sealing cup, (e) axial view of the interface between the sealing cup and the corroded pipe.

Table 3
Base condition set for FE modelling in this work.

Variable	Load			Pipe and corrosion defect					
	Cyclic loading		Internal pressure	Steel pipe			Corrosion defect (mm)		
	f	R	IP	R_p (mm)	t (mm)	Steel grade	d	L	W
Value	15 Hz	−0.6	8 MPa	458.8	8.1	X80	5.39	39.6	31.9

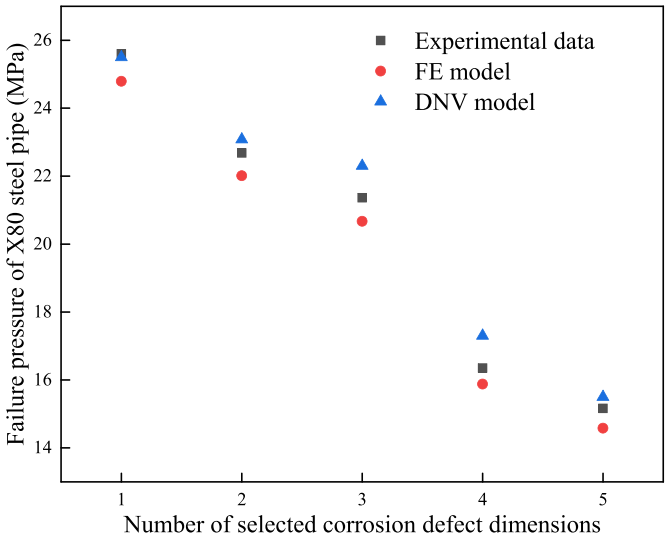

Fig. 4. Comparison of the modelling failure pressures compared with experimental testing data and the DNV modelling results.

et al., 2020).

2.3. Pipeline failure criterion

For modelling of the high- and low-grades of pipe steel, the Ramberg-Osgood (R–O) relationships used to describe the strain-hardening behavior of steels are given in Eqs. (2) and (3), respectively (Ramberg and Osgood, 1943):

$$\varepsilon = \frac{\sigma}{E} + K\left(\frac{\sigma}{\sigma_y}\right)^n \left(\frac{\sigma}{E}\right) \tag{2}$$

$$\varepsilon = \frac{\sigma}{E} + 0.079\left(\frac{\sigma}{\sigma_u}\right)^{12.64} \tag{3}$$

where ε is strain, σ is stress, E is Young's modulus, σ_y is yield strength, σ_u is ultimate tensile strength, and K and n are R–O material parameters, which are constants that depend on the materials to be modelled.

In this work, the failure criterion of the pipeline was based on stress criterion. Specifically, the pipeline fails when the equivalent von Mises stress exceeds a reference value at the corrosion defect. Of various methods for defect assessment of pipelines, such as ASME B31G, modified ASME B31G and DNV-RP-F101, the DNV model provides a relatively accurate method, as analyzed by Xu and Cheng (Xu and Cheng, 2012). The DNV model is defined by:

$$Q = \left(1 + 0.31\frac{L^2}{Dt}\right)^{\frac{1}{2}}$$

$$\mathrm{FP} = \frac{2t}{D-t}\sigma_u\left(\frac{1-\frac{d}{t}}{1-\frac{d}{tQ}}\right) \tag{4}$$

where Q is constant, and FP is failure pressure. The model uses the ultimate tensile strength of the steel as the reference stress level. Thus, σ_u was used to determine the pipeline failure, and the failure criterion was:

$$\sigma_{\mathrm{Mises}} = \frac{1}{\sqrt{2}}\sqrt{(\sigma_1-\sigma_2)^2 + (\sigma_2-\sigma_3)^2 + (\sigma_3-\sigma_1)^2} > [\sigma_u] \tag{5}$$

where σ_{Mises} is von Mises stress, and $\sigma_{1,2,3}$ refer to three principal stresses on the pipeline, i.e., hoop stress, longitudinal stress and radial stress, respectively.

Polyurethane with a Shore hardness of 95 A was selected as the sealing cup material of ILI tool contacting the inner surface of the pipe. The Young's modulus and Poisson's ratio of the material are 200 MPa

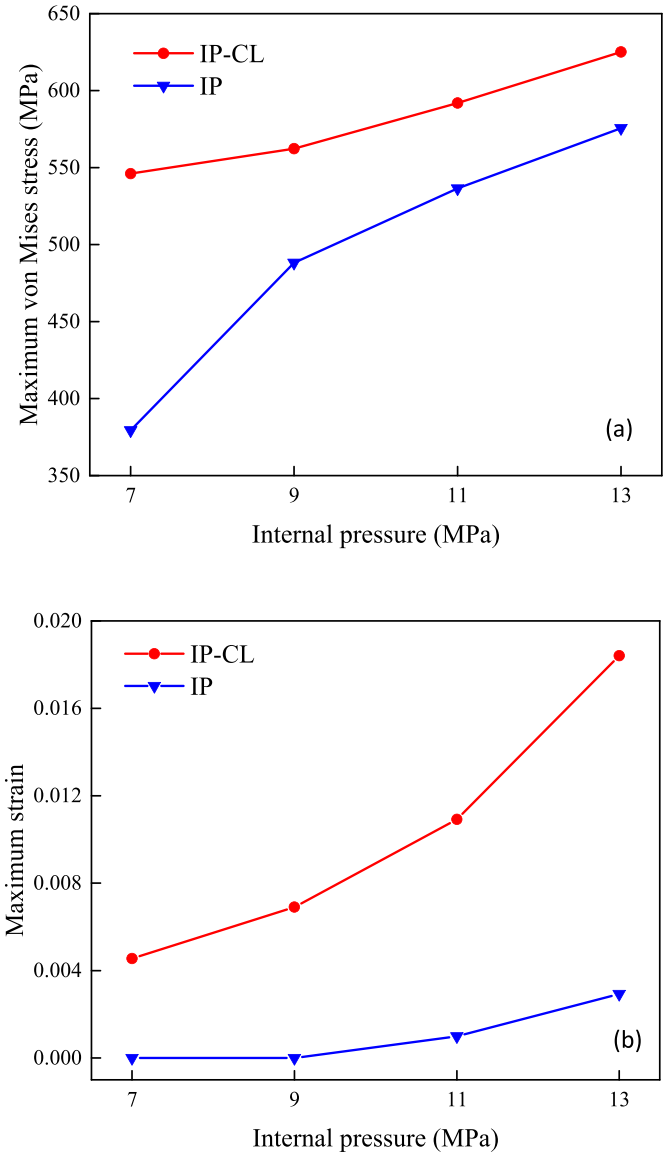

Fig. 5. The maximum (a) von Mises stress and (b) strain at the corrosion defect on X80 steel pipe under different internal pressures, where IP is internal pressure and CL is cyclic loading.

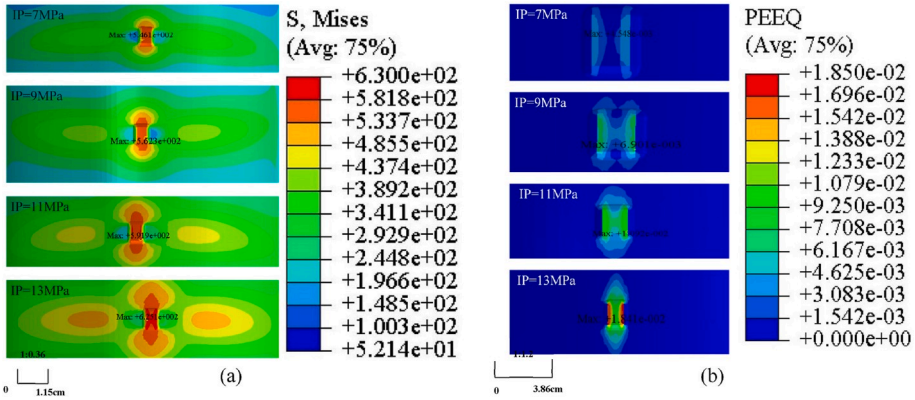

Fig. 6. Distributions of von Mises stress and strain at the corrosion defect on X80 steel pipe under the combined action of cyclic loading and different internal pressures (a) von Mises stress (MPa) contours, (b) strain contours. The scales of "1:0.36" and "1:1.2" refer to the ratios of the size of corrosion defect shown in the figure to the actual size of the defect.

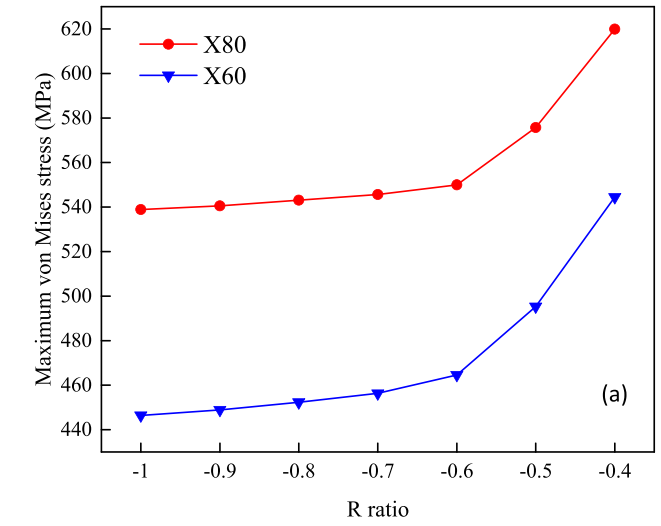

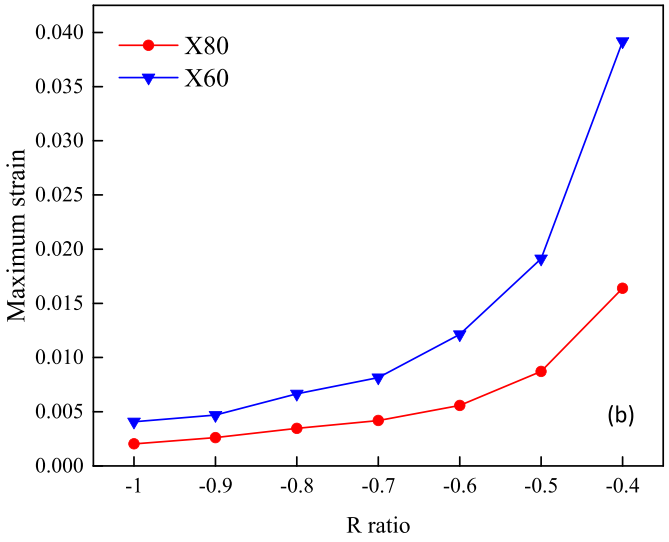

Fig. 7. Maximum (a) von Mises stress and (b) strain at the corrosion defect on X60 and X80 steels as a function of R-ratio of cyclic loading.

and 0.48, respectively.

2.4. Modelling validation

The modelling results can be validated by comparison with either theoretical calculations or experimental testing data. While experimental testing consumes time and resources, it is generally considered reliable. In this work, the modelling validation was conducted using the experimental data obtained on an X80 steel pipeline containing a single corrosion defect published by Benjamin and Cunha (2007). The outer diameter R_p of the pipe was 458.8 mm and the pipe wall thickness t was 8.1 mm. Five sets of corrosion defect dimension were used for verification, as shown in Table 2.

The DNV model was originally developed by fitting the modelling results with the field burst testing data obtained on different combinations of pipe geometry, pipeline steel and defect geometry. It was used as a reference to eliminate the contingency of experimental verification. The failure pressure derived from the developed model was also verified by the results obtained from DNV model.

2.5. FE modelling of the steel pipe containing a corrosion defect under cyclic loading

To model the cyclic loading induced by ILI tool operation in a natural gas pipeline, the movement speed of the tool was selected as 1 m/s, and the internal pressure (IP) was 7, 9, 11 and 13 MPa, respectively. The vibration of the tool was implemented by applying an acceleration on the modelled pipe interior as shown in Fig. 3, and the cyclic loading was applied on y-axis, i.e., the pipe wall thickness direction. Depending on acceleration and the load change of the ILI tool (Mohammad et al., 2007), the frequency, f, of the cyclic loading was set as 10, 15, 20 and 25 Hz (Zhang et al., 2015, 2017).

The stress ratio, R, of the cyclic loading was determined by:

$$R = \frac{\sigma_{min}}{\sigma_{max}} \quad (6)$$

where σ_{min} and σ_{max} are the minimum and maximum stresses, respectively. When R = −1, σ_{min} and σ_{max} have the same absolute value, but opposite directions, where the mean value is zero. The cyclic loading is called symmetrical relative to the zero-stress level. When R is not equal to −1, σ_{min} and σ_{max} have different absolute values and opposite directions. The mean value is not zero and the cyclic loading is not symmetrical about the zero-stress level. In this work, the R values to be modelled included −1, −0.9, −0.8, −0.7, −0.6, −0.5 and −0.4.

It is noted that the geometry of the corrosion defect changes as the corrosion progresses. Thus, the effect of the defect size was discussed to

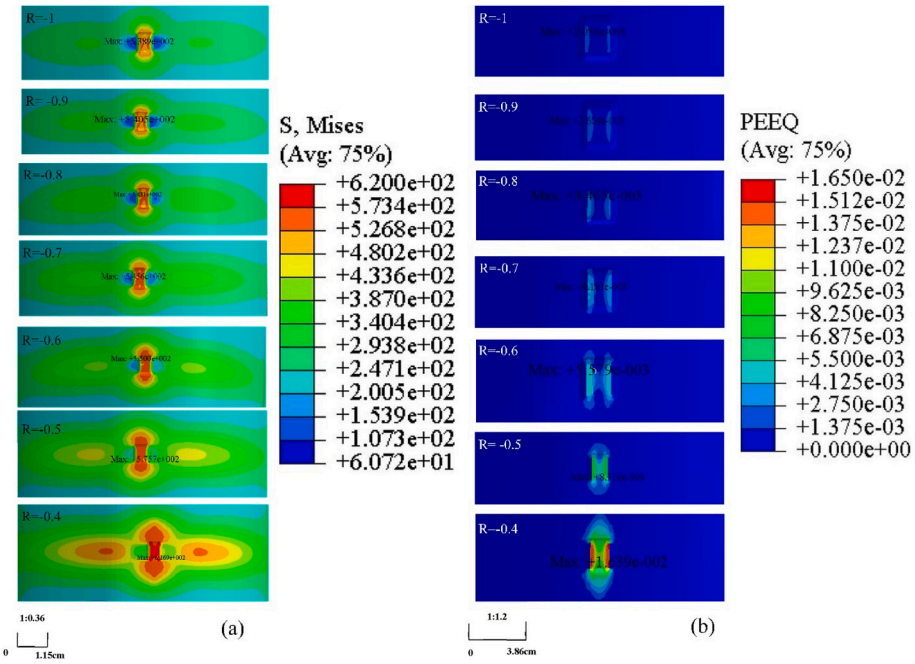

Fig. 8. Distributions of (a) von Mise stress (MPa), and (b) strain at the corrosion defect under the internal pressure (8 MPa) and cyclic loading with different R-ratios.

Table 4
Failure pressure of X80 steel pipe containing a corrosion defect under cyclic loading with different R-ratios.

R-ratio	−1	−0.9	−0.8	−0.7	−0.6	−0.5	−0.4
Failure pressure (MPa)	20.94	20.68	20.32	19.85	19.09	17.88	15.86

meet the actual needs. The authors' previous work demonstrated that the depth of a corrosion defect greatly affected the failure pressure of pipelines (Sun and Cheng, 2018). In this work, the width and length of the corrosion defect were fixed, and the corrosion depth d was set as 20% (1.62 mm), 40% (3.24 mm), 60% (4.86 mm) and 80% (6.48 mm) of the pipe wall thickness. The dimension selection of the modelled corrosion defects was based on the industry's corroded pipe database (Norske, 2004; Bipul and Mondal, 2016).

The single-factor analysis method was used to discuss the mechanical response under different conditions, while the pipe geometry remained unchanged. The base conditions used for FE modelling in this work are listed in Table 3.

3. Results and discussion

3.1. Comparison of the modelling results with testing data as published and the DNV results

A comparative analysis was performed to verify the reliability of the FE model developed in this work. It is noted that selections of the pipe steel, dimensions of corrosion defect and operating conditions ensure a sound base for comparison of the modelling results with experimental data. Fig. 4 shows the modelling failure pressures compared with the published experimental data (Benjamin and Cunha, 2007) and the DNV modelling results. The relative error (RE) between the experimental testing data and the FE modelling results is within 5%. Moreover, the RE of the FE modelling results compared with the DNV results is less than 8%. It is thus seen that the developed FE model can give reasonable results. Specifically, for X80 steel pipe containing a corrosion defect under the base conditions as listed in Table 3, the modelled failure pressure is 22.01 MPa. The burst test gave the failure pressure of 22.68 MPa according to the open publication (Benjamin and Cunha, 2007). The RE between them is 2.95% only, indicating a good consistence of the FE modelling result with the testing data. Furthermore, the failure pressure calculated by DNV model is 23.08 MPa. The RE between the modelled failure pressure and the DNV result is 4.64%, which again demonstrates the reliability of the developed model.

3.2. Local von Mises stress and strain distributions at corrosion defect under a combined action of internal pressure and cyclic loading: effect of internal pressure

The maximum von Mises stress and strain at the corrosion defect on X80 steel pipe under different internal pressures in the absence and presence of cyclic loading are shown in Fig. 5. It is seen that the presence of cyclic loading greatly increases the local von Mises stress and strain. As the internal pressure increases, both the von Mises stress and the strain increase. Under the internal pressures of 7 MPa and 9 MPa, the defect is in the elastic deformation stage. However, the addition of the cyclic loading makes the maximum stress at the corrosion defect exceed the yield stress even when the internal pressure is 7 MPa. In the absence of cyclic loading, the maximum stress is slightly higher than the yield stress when the internal pressure is up to 11 MPa, causing a plastic strain. Thus, the cyclic loading reduces the threshold internal pressure which causes a local plastic deformation at the corrosion defect on the pipeline.

Fig. 6 shows the von Mises stress and strain distributions at the corrosion defect on X80 steel pipe under cyclic loading and different internal pressures, where "Avg: 75%" refers to the default setting for data processing with a given accuracy in ABAQUS® software. It is noted that the unit of S, Mises is MPa, and PEEQ is dimensionless. It is seen that the stress concentration occurs at the corrosion defect, as highlighted in dark red (Fig. 6a). As the internal pressure increases, both the stress concentration and strain zones expand along the defect length direction. The stress in the direction of the defect width increases slightly with the internal pressure. When the internal pressure is 11 MPa and 13 MPa, the high stress zones are also found at both ends of the defect and the symmetrical sides in the circumferential direction. However, the stress level at these zones does not reach the yield stress, as colored in orange. The maximum strain still concentrates at the corrosion defect.

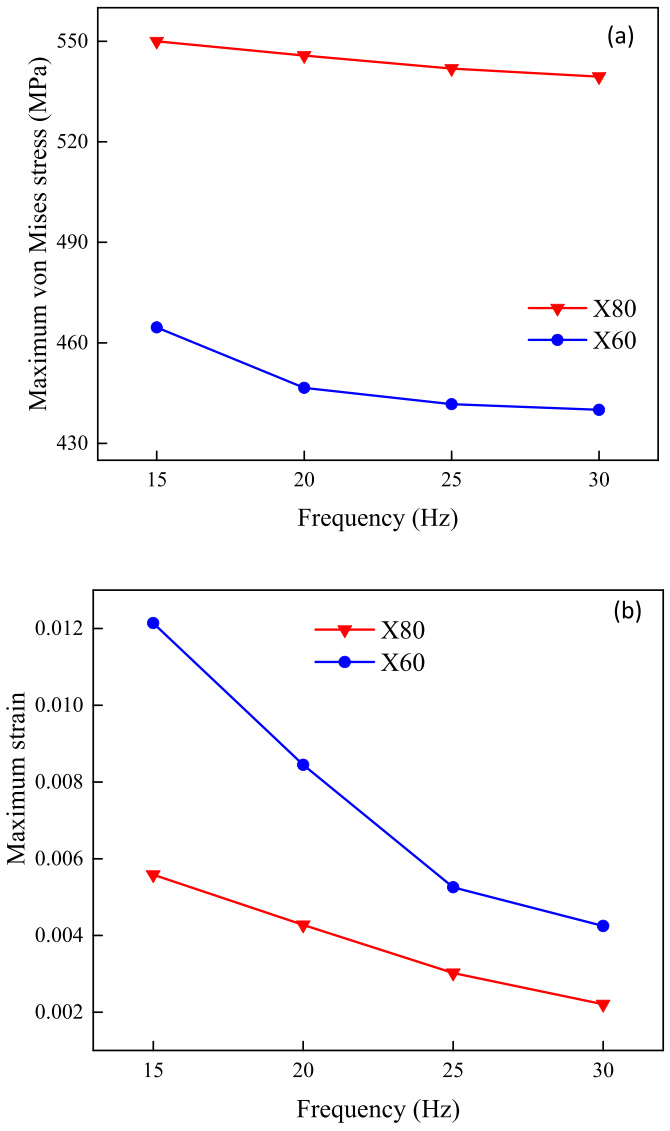

Fig. 9. The maximum (a) von Mises stress and (b) strain at a corrosion defect on X60 and X80 steel pipes under cyclic loading as a function of the frequency.

A comparison of the failure pressure of X80 steel pipeline containing a corrosion defect in the absence and presence cyclic loading under the base condition is conducted. The failure pressure of the pipeline under cyclic loading is 19.09 MPa, while it increases to 22.02 MPa in the absence of cyclic loading. Hence, the cyclic loading induced by ILI vibration can decrease the failure pressure of corroded pipelines. The results imply that, during ILI operation, the cyclic loading generated during the tool operation can adversely affect the safe operating pressure of the pipeline. The overlapped effect of the corrosion defect and the cyclic loading decreases the threshold internal pressure causing local plastic deformation.

3.3. Local von Mises stress and strain distributions at corrosion defect under a combined action of internal pressure and cyclic loading: effect of R-ratio

The maximum von Mises stress and maximum strain at the corrosion defect on X60 and X80 steels with different R-ratios during cyclic loading are shown in Fig. 7. As the R-ratio decreases, i.e., the difference between the minimum and maximum stresses increases, both the maximum von Mises stress and the maximum strain at the corrosion defect increase. At all R-ratios, the local stress concentration exceeds yield stress of the steels, indicating a local plastic deformation occurring at the corrosion defect. It is noted that the stress and strain increase rapidly when the R-ratio is below −0.6. Generally, the deformed defect under combined stresses can show multiple nonlinear characteristics (i.e., the material nonlinearity and geometry nonlinearity). This can cause the pressure-bearing capacity of the pipe to drop rapidly when the local stress exceeds a certain level. While there is a higher stress on X80 steel than on X60 steel at specific R-ratios, the strain on the X80 steel is lower.

Fig. 8 shows the stress and strain distributions at the corrosion defect on X80 steel pipeline under internal pressure of 8 MPa and cyclic loading with different R-ratios. It is seen that the stress concentration occurs at the defect. As the R-ratio decreases, the stress level at the defect increases. The stress concentration zone spreads along the defect length direction. The area of plastic deformation expands as well. It is noted that the stress level is always the highest at two edges of the defect, as shown in dark red.

Table 5
Failure pressure of X80 steel pipe containing a corrosion defect under cyclic loading with different frequencies.

Frequency (Hz)	15	20	25	30
Failure pressure (MPa)	19.09	19.83	20.57	20.93

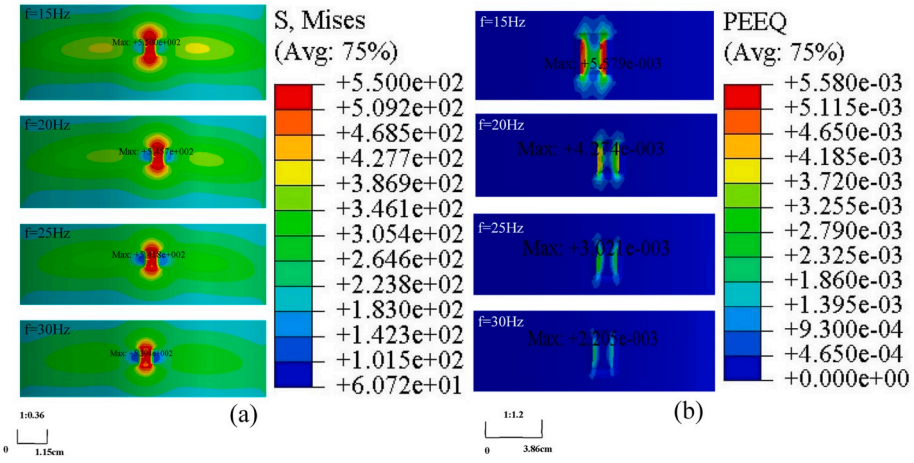

Fig. 10. Distributions of (a) von Mises stress (MPa) and (b) strain at the corrosion defect under the internal pressure (8 MPa) and cyclic loading with different frequencies.

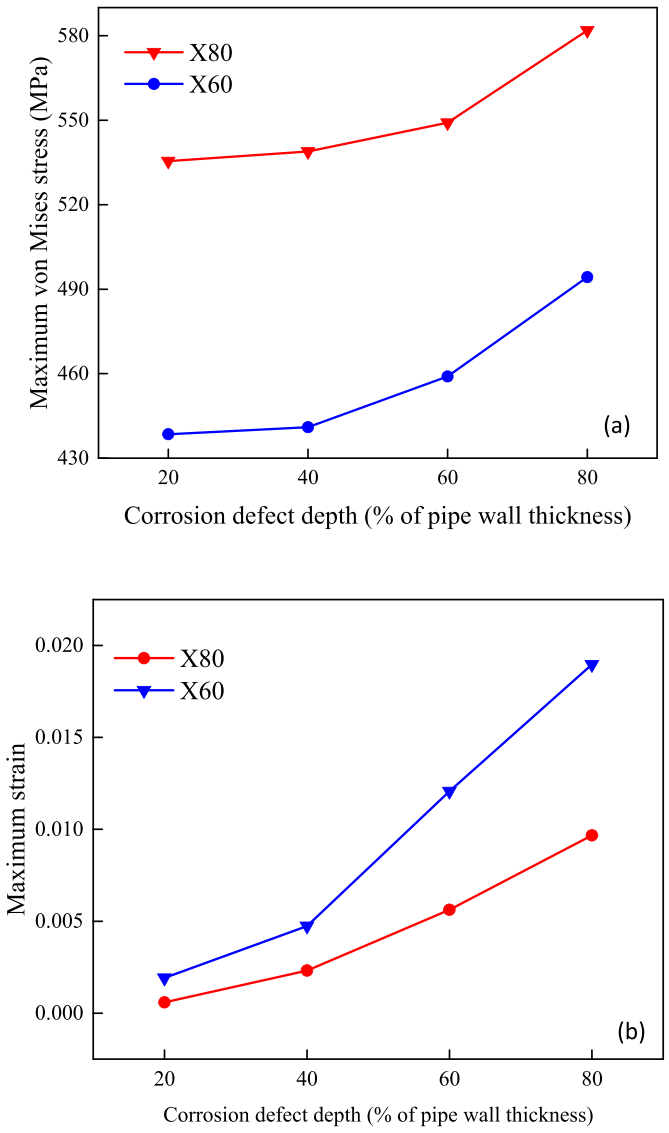

Fig. 11. The maximum (a) von Mises stress and (b) strain at the corrosion defect on X60 and X80 steel pipes as a function of the defect depth.

The R-ratio also affects the failure pressure of pipelines containing a corrosion defect. Table 4 shows the modelling failure pressure determined from Eq. (5) for X80 steel pipeline containing a corrosion defect under cyclic loading with different R-ratios. The results show that the failure pressure decreases slowly with the decrease of the R-ratio, and then drops rapidly when R-ratio is below −0.6.

3.4. Local von Mises stress and strain distributions at corrosion defect under a combined action of internal pressure and cyclic loading: effect of cyclic frequency

The maximum von Mises stress and strain at the corrosion defect on X60 and X80 steel pipes under cyclic loading with different frequencies are shown in Fig. 9. It is seen that both the von Mises stress and the strain decrease with increased frequency. The maximum von Mises stresses on both steels exceed the yield stress under the combined internal pressure and cyclic loading, resulting in a local plastic deformation. While X80 steel is associated with a higher von Mises stress than X60 steel, the latter possesses a higher local strain under identical conditions.

Fig. 10 shows the von Mises stress and strain distributions at the corrosion defect on X80 steel pipeline under internal pressure of 8 MPa and cyclic loading with different frequencies. It is seen that the stress concentration mainly occurs at the defect bottom. The stress level decreases with increased frequency. From the strain distribution, the maximum plastic deformation occurs at the defect base. The plastic deformation zone becomes smaller as the frequency increases.

The failure pressure of X80 steel pipe containing a corrosion defect as a function of the cyclic frequency is shown in Table 5. Generally, the failure pressure increases with the increased cyclic frequency. Thus, a low-frequency cyclic stress is likely to undermine the integrity of the pipeline.

3.5. Local von Mises stress and strain distributions at corrosion defect under a combined action of internal pressure and cyclic loading: effect of defect depth

The maximum von Mises stress and strain at the corrosion defect on X60 and X80 steel pipes with different defect depths are shown in Fig. 11. In general, the maximum von Mises stress and strain increase with increased depth of the corrosion defect. When the corrosion defect on X80 steel pipe increases from 20% to 80% of the pipe wall thickness, the maximum stress increases by 13.6 MPa and 32.8 MPa, respectively. For X60 steel, the dependence of the maximum von Mises stress on the

Table 6
Failure pressure of the corroded X80 steel pipe under cyclic loading as a function of the defect depth.

Defect depth (% of pipe wall thickness)	20	40	60	80
Failure pressure (MPa)	24.69	22.32	20.36	17.07

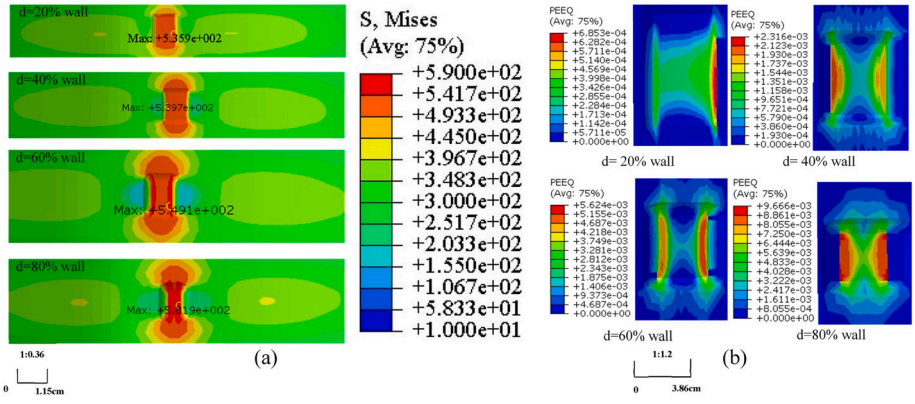

Fig. 12. Distributions of (a) von Mises stress (MPa) and (b) strain at the corrosion defect on X80 steel pipe under the internal pressure (8 MPa) and cyclic loading with different defect depths.

defect depth follows the same trend with X80 steel, but at a lower level.

Fig. 12 shows the von Mises stress and strain distributions at the corrosion defect on X80 steel pipe under the internal pressure of 8 MPa and cyclic loading with different defect depths. The von Mises stress is mainly concentrated at the defect bottom, as shown in dark red. The stress level increases with increased defect depth. Moreover, the stress concentration zone expands along the defect length direction, as shown in red. For the strain distribution, when the defect depth is 20% of the pipe wall thickness, the plastic deformation occurs at the base and edge of the corrosion defect. The yield area gradually expands as the defect depth increases.

Obviously, the depth of the corrosion defect greatly affects the local von Mises stress and strain distributions, and thus, the failure pressure of the pipeline. Table 6 shows the failure pressure of a corroded X80 steel pipe under cyclic loading as a function of the corrosion defect depth. It is seen that, as the corrosion defect becomes deeper along the wall thickness direction, the failure pressure decreases. The role of cyclic loading in pipeline failure is more important on severely corroded pipelines containing deep corrosion defects.

4. Conclusions and implication

A FE model is developed to simulate the local stress and strain distributions at corrosion defect on pressured gas pipelines which are under cyclic loading induced by vibration of ILI tool operation. The presence of cyclic loading greatly increases the local von Mises stress and strain at the corrosion defect, reducing the threshold internal pressure to cause local plastic deformation at the defect. As the internal pressure increases, both the von Mises stress and strain increase. The high stress/strain zones spread along the defect length direction. The local stress and strain at the corrosion defect increase with the decreased R-ratio and frequency of the cyclic loading, reducing the failure pressure of the pipeline. The increased defect depth would increase the local stress and strain concentrations at the defect and reduce the pipeline failure pressure.

ILI provides a reliable method for corrosion defect detection, location and sizing. Accurate analysis and assessment of ILI data has always been integral to the pipeline integrity management program. As stated, none of available defect assessment methods has considered the effect of cyclic loading induced by vibration of ILI tools on the local stress/strain distribution at the corrosion defects and thus the pipeline integrity. The research outcomes from this work can be used to determine the local stress and strain at corrosion defects with different dimensions (primarily the defect depths) under cyclic loading as a function of the R-ratio and frequency. At the same time, the failure pressure of the pipelines is predicted under the combined effect of corrosion defect and cyclic loading. In addition to a novel methodology for pipeline defect assessment developed in this work, determination of a quantitative relationship between the pipeline's failure pressure and the overlapped corrosion defect with cyclic loading would also provide the industry with important recommendations on safe operating condition (e.g., safe operating pressure) of corroded pipelines under ILI tool running. All of them are original and innovative, contributing to an improved pipeline integrity management.

Author statement

The first author, Guojin Qin, is a graduate student. He conducted all numerical modelling work, and performed the result analysis. He also drafted the manuscript.

The corresponding author, Dr. Frank Cheng, is the principal investigator of the project. He planned the scope of work and designed the research plan. He worked with the first author to analyze the results, and revised the manuscript for submission.

Declaration of competing interest

None.

Acknowledgement

This work was supported by China Scholarship Council (CSC no. 201908510201) and the University of Calgary.

Appendix A. Supplementary data

Supplementary data to this article can be found online at https://doi.org/10.1016/j.jngse.2020.103445.

References

Abdalla Filho, J.E., Machado, R.D., Bertin, R.J., Valentini, M.D., 2014. On the failure pressure of pipelines containing wall reduction and isolated pit corrosion defects. Comput. Struct. 132, 22–33.
American Petroleum Institute (Api), 2016. Fitness-For-Service (FFS) Evaluation. API 579-1, Washington DC, USA.
ASME (American Society of Mechanical Engineering), 1991. Manual for Determining the Remaining Strength of Corroded Pipelines. ASME B31G-1991, New York, USA.
Benjamin, A.C., Cunha, D.J.S., 2007. New method for the prediction of the failure pressure of interacting corrosion defects. In: Proc. The 17th Int. Offshore Polar Eng. Conf. (ISOPE)., pp. 3456–3465.
Chegeni, B., Jayasuriya, S., Das, S., 2019. Effect of corrosion on thin-walled pipes under combined internal pressure and bending. Thin-Walled Struct. 143, 106218.
Choi, J.B., Goo, B.K., Kim, J.C., Kim, Y.J., Kim, W.S., 2003. Development of limit load solutions for corroded gas pipelines. Int. J. Pres. Ves. Pip. 80, 121–128.
Gong, C., Zhou, W., 2017. First-order reliability method-based system reliability analyses of corroding pipelines considering multiple defects and failure modes. Struct. Infrastruct. Eng. 13, 1451–1461.
Gong, C., Zhou, W., 2018. Importance sampling-based system reliability analysis of corroding pipelines considering multiple failure modes. Reliab. Eng. Syst. Saf. 169, 199–208.
Ma, B., Shuai, J., Liu, D., Xu, K., 2013. Assessment on failure pressure of high strength pipeline with corrosion defects. Eng. Fail. Anal. 32, 209–219.
Mohammad, D., Amir, F., Ali, N., 2007. Investigation of dynamics and vibration of pig in oil and gas pipelines. ASME 2007 Int. Mech. Eng. Cong. Exp. 2015–2024.
Mondal, B.C., Dhar, A.S., 2019. Burst pressure of corroded pipelines considering combined axial forces and bending moments. Eng. Struct. 186, 43–51.
Norske, V.D., 2004. DNV Recommended Practice, RP-F10 (Corroded Pipelines).
Pluvinage, G., 2008. General approaches of pipeline defect assessment. In: Pluvinage, G., Elwany, M.H. (Eds.), Safety, Reliability and Risks Associated with Water, Oil and Gas Pipelines. NATO Science for Peace and Security Series. Springer, Dordrecht.
Ramberg, W., Osgood, W.R., 1943. Description of Stress–Strain Curves by Three Parameters. Technical Note No. 902. National Advisory Committee for Aeronautics, Washington DC.
Sun, J.L., Cheng, Y.F., 2018. Assessment by finite element modeling of the interaction of multiple corrosion defects and the effect on failure pressure of corroded pipelines. Eng. Struct. 165, 278–286.
Sun, J.L., Cheng, Y.F., 2019a. Modelling of mechano-electrochemical interaction of multiple longitudinally aligned corrosion defects on oil/gas pipelines. Eng. Struct. 190, 9–19.
Sun, J.L., Cheng, Y.F., 2019b. Investigation by numerical modeling of the mechano-electrochemical interaction of circumferentially aligned corrosion defects on pipelines. Thin-Walled Struct. 144, 106314.
Systemes, D., 2015. ABAQUS 6.14 Documentation–Theory Guide.
Vanaei, H.R., Eslami, A., Egbewande, A., 2017. A review on pipeline corrosion, in-line inspection (ILI), and corrosion growth rate models. Int. J. Pres. Ves. Pip. 149, 43–54.
Wu, Y., Li, J., 2019. Finite element analysis on mechanical behavior of semi-exposed pipeline subjected to debris flows. Eng. Fail. Anal. 105, 781–797.
Xu, L.Y., Cheng, Y.F., 2012. Reliability and failure pressure prediction of various grades of pipeline steel in the presence of corrosion defects and pre-strain. Int. J. Pres. Ves. Pip. 89, 75–84.
Xu, L.Y., Cheng, Y.F., 2013. Development of a finite element model for simulation and prediction of mechano-electrochemical effect of pipeline corrosion. Corrosion Sci. 73, 150–160.
Xu, L.Y., Cheng, Y.F., 2017. A finite element based model for prediction of corrosion defect growth on pipelines. Int. J. Pres. Ves. Pip. 153, 70–79.
Zhang, H., Zhang, S., Liu, S., Zhu, X., Tang, B., 2015. Chatter vibration phenomenon of pipeline inspection gauges (PIGs) in natural gas pipeline. J. Nat. Gas Sci. Eng. 27, 1129–1140.
Zhang, H., Zhang, S., Liu, L., Wang, Y., 2017. Collisional vibration of PIGs (pipeline inspection gauges) passing through girth welds in pipelines. J. Nat. Gas Sci. Eng. 37, 15–28.
Zhang, H., Dong, J., Cui, C., Liu, S., 2020. Stress and strain analysis of spherical sealing cups of fluid-driven pipeline robot in dented oil and gas pipeline. Eng. Fail. Anal. 108, 104294.